Solution-Synthesized High-Mobility Tellurium Nanoflakes for Short-Wave Infrared Photodetectors

Matin Amani, [#,1,2], Chaoliang Tan [#,1,2], George Zhang[1,2], Chunsong Zhao[1,2,3], James Bullock[1,2], Xiaohui Song[3,4], Hyungjin Kim[1,2], Vivek Raj Shrestha[5], Yang Gao[6], Kenneth B. Crozier[5,6], Mary Scott[3,4], and Ali Javey[1,2,]*

[1]Electrical Engineering and Computer Sciences, University of California at Berkeley, Berkeley, CA 94720, United States
[2]Materials Sciences Division, Lawrence Berkeley National Laboratory, Berkeley, CA 94720, United States
[3]Department of Materials Science and Engineering, University of California at Berkeley, Berkeley, CA 94720, United States
[4]The Molecular Foundry, Lawrence Berkeley National Laboratory, Berkeley, CA, 94720
[5]School of Physics, University of Melbourne, VIC 3010, Australia
[6]Department of Electrical and Electronic Engineering, University of Melbourne, Victoria 3010, Australia

*Address correspondence to ajavey@eecs.berkeley.edu
[#]These authors contribute equally to this work.

Keywords: tellurium, 2D materials, solution-synthesized, high-mobility, short-wave infrared, photodetectors

Abstract

Two-dimensional (2D) materials, particularly black phosphorous (bP), have demonstrated themselves to be excellent candidates for high-performance infrared photodetectors and transistors. However, high-quality bP can be only obtained *via* mechanical exfoliation from high temperature- and high-pressure-grown bulk crystals and degrades rapidly when exposed to ambient conditions. Here, we report solution-synthesized and air-stable quasi-2D tellurium (Te) nanoflakes for short-wave infrared (SWIR) photodetectors. We

perform comprehensive optical characterization *via* polarization-resolved transmission and reflection measurements, and report the absorbance and complex refractive index of Te crystals. It is found that this material is an indirect semiconductor with a bandgap of 0.31 eV. From temperature-dependent electrical measurements, we confirm this bandgap value and find that 12 nm thick Te nanoflake show high hole mobilities of 450 and 1430 $cm^2 V^{-1} s^{-1}$ at 300K and 77K, respectively. Finally, we demonstrate that despite its indirect bandgap, Te can be utilized for high-performance SWIR photodetectors by employing optical cavity substrates consisting of Au/Al_2O_3 to dramatically increase the absorption in the semiconductor. By changing the thickness of the Al_2O_3 cavity, the peak responsivity of Te photoconductors can be tuned from 1.4 µm (13 A/W) to 2.4 µm (8 A/W) with a cut-off wavelength of 3.4 µm, fully capturing the SWIR band. An optimized room temperature specific detectivity (D*) of 2×10^9 cm $Hz^{1/2} W^{-1}$ is obtained at a wavelength of 1.7 µm.

Narrow bandgap semiconductors, with bandgaps in the range of 0.7 to 0.3 eV, have been heavily investigated for numerous applications. These include high-speed and high-performance transistors, which typically require materials with high mobility and low effective mass.[1,2] Additionally, photodetectors and light sources which can operate in the short-wave infrared (SWIR, 1.4 µm – 3 µm) band are heavily utilized for imaging and optical communication.[3-5] This area has typically been dominated by III-V semiconductors such as indium gallium arsenide (InGaAs) and indium

58 gallium arsenide phosphide (InGaAsP), which have excellent performance but
59 require complex growth and fabrication procedures.[6,7] Numerous research
60 groups have investigated techniques to achieve III-V semiconductors through
61 non-epitaxial growth on silicon or by layer transfer.[8-11] However, these
62 techniques still introduce significant complexity and may require high growth
63 temperature. Moreover, key limitations still exist in InGaAs-based devices; an
64 example being edge-recombination in scaled InGaAs photodiodes which
65 limits pixel sizes in focal plane arrays to dimensions of 5-6 μm, well above
66 the diffraction limit.[12] As such, there is a pressing need to find suitable
67 materials that can either improve the performance and/or reduce the costs
68 of these devices.

69 One such potential material system is two-dimensional (2D) materials,
70 which have been heavily studied over the past decade. One of the key
71 advantages of 2D materials, which enables their high performance, is their
72 naturally terminated surfaces; *i.e.* since the out-of-plane bonds in these
73 materials are van der Waals rather than covalent.[13,14] As such, they do not
74 suffer from the surface-induced performance degradation commonly
75 observed in three-dimensional (3D) semiconductors, which require surface
76 passivation (typically in the form of cladding layers). This has enabled
77 extraordinary electronic and optical properties of these materials such as
78 photoluminescence quantum yields approaching unity and their exceptional
79 thickness scalability down to the monolayer limit.[15,16] Devices which have
80 exploited the advantages and physics of 2D systems have demonstrated
81 dramatic scaling as well as new devices paradigms.[17-19] However, edges in 2D

82 layers still act as recombination centers and are analogous to a surface in a
83 3D crystal structure.[20] A recent work by Wang *et al.* demonstrated the
84 solution synthesis of air-stable quasi-2D Te nanosheets and its high-
85 performance for field-effect transistors.[21] Note that Te is a true one-
86 dimensional (1D) system, which can potentially overcome some of these
87 limitations since it consists of van der Waals bonded molecular chains.[22] As
88 such these material systems naturally possess no dangling bonds when
89 scaled, with the exception of the ends of the molecular chains.[22] Importantly,
90 this material also possesses a small, thickness tunable bandgap enabling its
91 potential use in SWIR photodetectors. Recent theoretical works have
92 predicated an indirect gap of 0.35 eV in bulk and a direct gap of 1.04 eV in
93 the monolayer case.[23,24]

94 Here, we systematically study the optical and electrical properties of
95 solution-synthesized quasi-2D Te nanoflakes. From polarization-resolved IR
96 transmission and reflection measurements, we experimentally extract the
97 bandgap, absorbance, and complex refractive index of this material.
98 Temperature-dependent electrical measurements were performed to verify
99 the optically measured bandgap values as well as determine the carrier
100 transport properties as a function of temperature in quasi-2D Te nanoflakes.
101 Finally, we demonstrate SWIR photoconductive detectors based on thin (16-
102 20 nm) quasi-2D Te nanoflakes. Although this material has low absorbance in
103 the SWIR (6×10^5 cm^{-1} for wavelengths in the range of 2 to 3.5 μm) induced
104 by the indirect bandgap, the Te nanoflake-based photodetectors exhibit high
105 photoresponsivity and specific detectivity by leveraging optical cavities

106 engineered to maximize absorption at various technologically important
107 wavelengths in the SWIR range.

108 **RESULTS and DISCUSSION**

109 **Material Synthesis and Characterization.**

110 Quasi-2D Te nanoflakes with varying thickness in the range of 10-200
111 nm were synthesized by a hydrothermal method *via* reduction of sodium
112 tellurite with hydrazine hydrate in the presence of poly(-vinyl pyrrolidone) in
113 an aqueous alkaline solution at 180℃ for certain varying times (details are
114 provided in methods).[21,25] The crystal structure of Te is shown in Figure 1a-c.
115 The Te crystallizes in a structure composed of Te atomic chains in a
116 triangular helix that are stacked together *via* van der Waals forces in a
117 hexagonal array (Figure 1a). In this structure, Te atoms only form covalent
118 bonds to the two nearest neighbor Te atoms in the helical chain (Figure 1b).
119 Therefore, Te is a true 1D system rather than a 2D van der Waals crystal.
120 When it is viewed from x-axis, the zig-zag layers are seen to be stacked
121 together *via* van der Waals forces to form a 3D structure (Figure 1c). Figure
122 1d shows the transmission electron microscope (TEM) image of a typical Te
123 nanoflake with a length of 15 μm and width of 4 μm. The corresponding high-
124 resolution TEM (HR-TEM) image shows the continuous crystal lattice of the Te
125 nanoflake and the measured the lattice constant is ~2 Å (Figure 1e), which is
126 assignable to the (003) planes of the Te crystal. The corresponding selected
127 area electron diffraction (SAED) pattern of the Te nanoflake shows bright
128 diffraction spots with a rectangular shape, in which the nearest two spots to

129 the diffraction center correspond to the (110) and (001) planes of the Te
130 crystal (Figure 1f). Both the HR-TEM and SAED pattern results indicate that
131 the solution-synthesized Te nanoflake is single-crystalline. The optical image
132 shows that Te nanoflakes have an irregular shape with length of tens of
133 micrometers, width of few micrometers and thickness of 10-30 nm (Figure
134 2a). Note that there are always some Te nanowires along Te nanoflakes in
135 the growth solution, but Te nanowires can be partially removed from the
136 solution by proper centrifugation (see the details in Methods). An atomic
137 force microscope (AFM) image of a Te nanoflake with a thickness of 16.1 nm
138 is shown in Figure 2b. Raman spectrum of tellurium nanoflakes gives three
139 vibrational modes at 92, 121, 141 cm^{-1} (Figure 2c) corresponding to the E_1-
140 TO, A_1, and E_2 peaks, which are consistent with previous literature
141 reports.[21,26] The X-ray diffraction (XRD) peaks of Te nanoflakes match well
142 with the simulated reference (Figure 2d). Both Raman and XRD analysis
143 further confirm the successful preparation of Te nanoflakes.[21,25]

144 **Electrical Properties.**

145 We now turn our attention to the electrical properties and performance
146 of the quasi-2D Te nanoflakes. To this end, back-gated field-effect transistors
147 were fabricated on Si/50 nm SiO_2 by patterning Pd (40 nm thick) electrodes
148 on Te nanoflakes with thickness ranging from 10-20 nm using electron-beam
149 lithography.[21] The I_d-V_d characteristics of a 12.3 nm thick quasi-2D Te field-
150 effect transistor, as well as an optical image of the measured device (L = 6.8
151 μm, W = 1.5 μm, where L and W are length and width respectively) are
152 shown in Figure 3a. The device shows dominantly p-type transport

153 characteristics and a peak current density of 116 μA/μm at a V_d = -1 V and V_g
154 = -20 V. It should be noted that in some devices (Figure S1) ambipolar
155 transport characteristics are observed, indicating that *via* proper contact
156 engineering n-type transport could be obtained. Additionally, this device
157 shows a current on/off ratio of ~3×10^3, which is expected for a material with
158 a small bulk bandgap of ~0.31 eV. The output characteristics of this device
159 are shown in Figure 3b, and show current saturation at high drain bias, as
160 well as linear behavior at low drain biases, indicating low contact resistance.
161 We then utilize the square law model to calculate the effective mobility (μ_{Eff})
162 in this device as a function of gate field (Figure 3c) using $\mu_{Eff}=\left(dI_d/dV_d\right)/$¿¿,
163 where C_{ox} is the gate capacitance (69.1 nF cm^{-2} in the case of 50 nm SiO_2)
164 and V_t is the threshold voltage. We extract a high peak μ_{Eff} of 619 $cm^2V^{-1}s^{-1}$
165 for holes, which is very competitive with high-performance p-type
166 semiconductors with similar bandgaps such as InGaSb and bP, especially
167 considering that the material is prepared by a solution-based method.[27-29]
168 The thickness-dependent transport properties of quasi-2D Te nanoflakes
169 were also investigated over a range of 11 to 36 nm as shown in Figure 3d
170 and 3e. As the overall thickness of the Te nanoflakes is reduced a dramatic
171 improvement in the ratio of the on/off currents from ~30× to ~4000× can be
172 observed, which can be attributed to reduced gating efficiency in the device.
173 Furthermore, over this measured thickness range, we find that there is
174 negligible variation in the peak effective mobility which has an average value
175 of 424±74 $cm^2V^{-1}s^{-1}$ over thirty-nine measured samples.

176 To better understand the transport in this material, we performed
177 temperature-dependent electrical characterization of the devices. I_d-V_g
178 characteristics of quasi-2D Te nanoflakes with different thicknesses
179 measured over a temperature range of 77K to 350K are shown in Figure 4a
180 and Figure S1. A clear increase in the current on/off ratio can be observed
181 when the device is cooled, which is consistent with small bandgap materials,
182 where thermal generation dramatically increases the carrier densities at
183 elevated temperatures. From the temperature-dependent measurements, we
184 extract the μ_{Eff} at a gate overdrive of -10 V as a function of temperature for
185 different layer thicknesses as shown in Figure 4b. For all thicknesses, the
186 mobility increases as the temperature is reduced, with the 12 nm thick
187 device showing a μ_{Eff} of 1430 and 450 $cm^2V^{-1}s^{-1}$ at 77K and 300K respectively.
188 For all three thicknesses, we observe the temperature dependence of
189 mobility can be fitted with a power law, $\mu_{Eff} \propto T^{-\gamma}$, where γ = -1.03 in our case.
190 This indicates that the mobility in this material is limited by phonon
191 scattering and not ionized impurities.[30] Additionally, we estimate the
192 bandgap using temperature-dependent measurements on a device prepared
193 on a 260 nm gate oxide. In this case, the minimum drain currents, $I_{d,min}$, is
194 determined by thermal activation of carriers over the contact Schottky
195 barrier height.[31] The resulting data, shown in Figure 4c, can be fit using:
196 $I_{d,min} \propto \exp\left(-E_g/kT\right)$
197 where T is the temperature, E_g is the transport bandgap, and k is the
198 Boltzmann constant. We extract an E_g of 280 meV for a 11.8 nm thick

199 sample, and it is important to note that this method is expected to
200 underestimate the bandgap due to contributions from trap states.

201 **Optical Properties.**

202 To identify the optical bandgap of the quasi-2D Te nanoflakes, we
203 performed polarization-resolved transmission and reflection measurements
204 on Te nanoflakes which were transferred onto KBr. Polarization-resolved
205 transmission and reflection spectra measured on a 111 nm thick sample are
206 shown in Figure 5a. In order to accurately extract the absorption in the
207 sample, the optical path was kept constant for both the transmission and
208 reflection measurements, as annotated in the Figure 5a. Transmission and
209 reflection spectra were taken in reference to the blank KBr substrate and an
210 Au mirror, respectively. The total absorption and the corresponding
211 absorption coefficient in the material can then be calculated as 100%-
212 Reflection-Transmission as shown in Figure 5b and 5c. For light polarized
213 along the direction of the Te molecular wires (defined as 90°), we measure a
214 strong absorption that can be fitted to a direct bandgap (Figure 5c and
215 Figure S2) at 0.71 eV. However, when the light is polarized perpendicular to
216 the axis of the Te molecular wires (defined as 0°) a significantly weaker
217 absorption edge is observed at lower wavelengths. From similar analysis, the
218 transition can be fitted to an indirect bandgap at 0.31 eV. Importantly, while
219 the absorption coefficient for wavelengths below 1.6 μm is high (4.5×10^6 cm^{-1}
220), the absorption for longer wavelengths (1.6 μm < λ < 3.4 μm) is an order
221 of magnitude lower (6×10^5 cm^{-1}). As such, in order to effectively utilize this

material in the full SWIR band, it is necessary to increase the absorption *via* proper optical engineering.[32]

To this end, we extracted the complex refractive index (n, k) which can be used to estimate the total absorption in the quasi-2D Te layers in combination with optical cavities, back-reflectors, or anti-reflection coatings. The refractive index was extracted using a previously established technique for nanoscale materials for unpolarized light, where reflection is measured as a function of oxide or sample thickness.[33] In our case, quasi-2D Te nanoflakes of thicknesses varying from 16 nm to 180 nm were drop-casted on Au substrates, and the reflection spectra were measured using an Fourier transform infrared spectrometer (FTIR). The resulting reflection data are plotted as a function of thickness and wavelength. (Figure 6a and Figure S3). To extract the complex refractive index from the reflection measurements, we utilize the transfer matrix method to fit a refractive index to the measured reflection *versus* thickness at each wavelength.[34] The extracted n and k values are plotted in Figure 6b; the extracted extinction coefficient clearly shows absorption resulting from both the indirect and direct transitions at the expected wavelengths and corroborates the results from absorption measurements shown in Figure 5c.

Optical Cavity Enhanced Gated-Photoconductors.

Based on the optical properties and electrical properties of quasi-2D Te, the device structure shown in Figure 7a was chosen to optimize photoconductive detectors targeting the SWIR spectrum. Here, we selected thicknesses in the range of 16-20 nm for the quasi-2D Te layers, which

246 provides desired electrical characteristics, the most important of which
247 being a low dark current.[35] To increase the absorption, an optical cavity
248 consisting of an optically thick Au film (100 nm) and an Al_2O_3 dielectric
249 spacer layer was utilized. The predicted absorption for an 18 nm thick Te
250 layer as a function of wavelength and Al_2O_3 thickness was calculated using
251 the transfer matrix method and is shown in Figure 7b. From these
252 simulations, it can be clearly seen that by adjusting the thickness of the Al_2O_3
253 layer, the peak absorption wavelength can be tuned over a large range and
254 the total absorption in the material can be increased by over two orders of
255 magnitude relative to a sample on Si/SiO_2 (Figure S4). Additionally, the
256 optical cavity simultaneously acts as the gate stack in this structure.

257 Figure 7c shows optical images of devices fabricated on three different
258 Al_2O_3 spacer thickness (550 nm (i), 150 nm (ii), and 350 nm (iii)), which are
259 selected to provide optimized absorption at 1.4 μm, 1.8 μm, and 2.2 μm,
260 respectively (reflection spectra of devices on these substrates are shown in
261 Figure S5). The spectral responsivity of these devices to SWIR illumination
262 was characterized using an FTIR, by placing the devices in place of the
263 internal detector and focusing the light source of the FTIR on the device with
264 a CaF_2 lens. To calibrate the measurements, the internal Deuterated
265 Triglycine Sulfate (DTGS) in the FTIR, which has a wavelength independent
266 responsivity, was used to determine the relative intensity of the light source
267 while a NIST traceable Ge photodiode was used to determine the absolute
268 intensity of the illumination (further measurement details are provided in the
269 methods and ref. 35). The final responsivity (R) is then calculated as $R(\lambda)$ =

270 $I_{ph}(\lambda)/P_{in}(\lambda)$, where I_{ph} is the photocurrent and P_{in} is the incident optical power
271 on the device. The spectral responsivity for representative devices fabricated
272 on the three different optical cavity substrates are shown in Figure 7d.
273 Devices fabricated on these three substrates were measured at a drain bias
274 of V_d = 5 V, and the gate voltage was adjusted to maximize the responsivity.
275 The measured responsivity curves closely match the calculated absorption
276 curves which further confirms the estimated refractive index values.

277 **Gate-dependent Photoresponse, Detectivity, and Frequency**
278 **Response.**

279 To further characterize the performance of these photodetectors,
280 additional measurements were performed on an 18.8 nm thick device
281 fabricated on a Au/150 nm Al_2O_3 substrate. The I_d-V_g characteristics of a
282 device measured at 78K and 297K without the presence of a cold shield is
283 shown in Figure 8a. The gate and drain bias dependence of the device at an
284 incident wavelength of 1.7 µm are shown in Figure 8b and 8c, respectively.
285 We can see that the photoresponse can be strongly modulated by the gate
286 bias and is maximized when the device is biased such that drain current is
287 minimized, similar to what has previously been observed in bP
288 photoconductors[35,36]. This can be seen in the clear peak responsivity of 27 A/
289 W at 78K, while the responsivity at 297K saturates with increasing gate
290 biases to a peak measured value of 16 A/W. Additionally, the device shows
291 an approximately linearly increasing responsivity at low V_d, and begins to
292 show saturation at high V_d. The full spectral responsivity of the device is

293 shown in Figure 8d. For V_d = 5 V, this detector shows a peak responsivity at λ
294 = 1.7 μm of 27 A/W and 16 A/W at 78K and 297K, respectively.

295 To calculate the specific detectivity of this device, the noise current
296 density is measured under bias conditions which give maximum responsivity
297 at an integration time (Δf) of one second and is shown in Figure 8e. The
298 noise currents clearly show the expected $1/f$ (where f is frequency) flicker
299 noise which is typically attributed to charge trapping/de-trapping. Utilizing
300 the noise and responsivity measurements, we calculate the specific
301 detectivity (D^*) using:

302 $$D^{¿}=\frac{\sqrt{A\Delta f}}{NEP}=\frac{R\sqrt{A\Delta f}}{i_n}$$

303 where A is the detector area, NEP is noise equivalent power, and i_n is the
304 noise current. In the ideal case for photoconductors, the i_n is limited by shot
305 noise and can be calculated from dark current using: $\langle i_S^2\rangle=2qI_{G-R}\Delta f$.[37,38] This
306 typically overestimates noise current; thus, we utilized the experimental
307 noise currents taken at a modulation frequency of 1 kHz, which was selected
308 to minimize the contribution of $1/f$ noise. The specific detectivity as a
309 function of wavelength is shown in Figure 8f for both 78K and 297K. At room
310 temperature these devices show a peak D* of 2.9×10^9 cmHz$^{1/2}$W^{-1}. This value
311 dramatically increases at low temperatures due to the large decrease in the
312 noise current as well as the improved responsivity to a peak value of
313 2.6×10^{11} cmHz$^{1/2}$W^{-1}.

314 To characterize the speed of this device, a directly modulated laser
315 diode (λ = 1.55 μm) was utilized to excite the photoconductor. The response

of the device to a low-frequency and high-frequency square wave are shown in Figure 9a and 9b, respectively. From both of the step responses shown in Figure 9a and 9b, a slow and fast component of the rise/fall time can be observed. To more clearly characterize this behavior, the photoresponse was measured with a sinusoidally modulated incident light over a wide frequency range (100 mHz to 100 kHz) as shown in Figure 9c. Over this measured spectral range, a clear 3dB cutoff wavelength cannot be observed, indicating that it is higher than the measured range. However, the device shows a weak increase in response for light modulated at low frequencies; *i.e.* the photoresponse at a 100 kHz shows only a ~5× drop relative to the low frequency (~0.1 Hz) photoresponse. It is likely that this behavior is a result of photoconductive gain present in the device which consistent with the high responsivity and the short carrier transit time (τ_{tr}), which is calculated to be 0.4 ns according to $\tau_{tr} = L^2/(\mu V_d)$, where L is channel length (8.9 μm) and μ in this case is 392 $cm^2V^{-1}s^{-1}$. The exact mechanisms of the gain likely is a result of the population and depopulation of trap states, which show saturation at high illumination powers.[39-41] This is particularly likely given the fact that the Te nanoflakes in this work were prepared using solution-based synthesis.

Polarization-Resolved Photoresponse.

Finally, we investigated the polarization-dependent photoresponse of Te nanoflake-based photodetectors. We chose a device fabricated on a 350 nm thick Al_2O_3 substrate as an example to measure the responsivity, which provides strong absorption enhancement at wavelengths covering indirect gap band edge. Figure 10a shows the responsivity of an 18.8 nm thick Te

340 photoconductor measured at various incident polarization angles, with 0° 341 and 90° corresponding to light polarized perpendicular and parallel to the 342 molecular wires, respectively. A clear drop in the responsivity for 343 wavelengths greater 1.5 μm can be observed when the incident light is 344 polarized at 90°, consistent with the indirect band edge. A polar plot showing 345 the responsivity as a function of polarization at wavelengths of 3 μm and 1.5 346 μm is shown in Figure 10b, and clearly shows the highly anisotropic 347 responsivity of the indirect gap, while the direct gap shows minimal 348 dependence on the polarization of the light.

349 **CONCLUSION**

350 In summary, we have performed a systematic study on the electrical 351 and optical properties of solution-synthesized quasi-2D Te, an indirect, small 352 bandgap (0.31 eV) semiconductor. The Te nanoflake-transistor shows high 353 effective hole mobilities of 450 and 1430 $cm^2 V^{-1} s^{-1}$ at 300K and 77K 354 respectively. The absorbance and complex refractive index of Te were also 355 extracted based on the polarization-resolved transmission and reflection 356 measurements. Furthermore, the Te gated photodetectors exhibit high 357 responsivities over the entire SWIR range with a cut-off wavelength of 3.4 358 μm. Importantly, using the extracted optical parameters, we dramatically 359 enhanced the responsivity and specific detectivity of Te photodetectors 360 using optical cavity substrates. We show that the peak wavelength can be 361 tuned from 1.4 to 2.4 μm by changing the thickness of the Al_2O_3 cavity on 362 Au. This simple substrate engineering technique can be a general way to 363 significantly enhance the performance of other 2D material-based

photodetectors. In addition, due to the anisotropic crystal structure of the Te nanoflakes, the devices possess a polarization-sensitive SWIR photoresponse. Our electrical and optoelectronic study indicate that Te is a promising material for high-performance and low-cost electronic and optoelectronic devices. Finally, this material has a high potential for wafer-scale production either through the assembly of solution-processed nanoflakes to form semi-continuous thin films or through techniques such as chemical vapor deposition or epitaxial growth.

METHODS

Chemicals

Sodium tellurite (Na_2TeO_3), hydrazine monohydrate ($N_2H_4 \bullet H_20$) and ammonium hydroxide solution ($NH_3 \bullet H_20$, 28%) were purchased from Sigma-Aldrich (USA). Poly(-vinyl pyrrolidone) (PVP, average M.W. 58,000) was purchased from Alfa Aesar (USA). All the chemicals were used as received without further purification. Milli-Q water (Milli-Q System, Millipore) was used in all experiments.

Synthesis of tellurium nanoflakes

Tellurium nanoflakes were synthesized by a hydrothermal method according to a previously reported procedure with slight modifications.[21,25] In a typical procedure, 1.5 g of PVP was first dissolved in 16 mL DI water and 46 mg of Na_2TeO_3 was then added and dissolved into the PVP solution to form a clear solution. Then, 1.66 mL of ammonium hydroxide solution and 0.838 mL of hydrazine monohydrate was added into the above solution in sequence. The solution was then transferred into a 25 mL Teflon-lined stainless steel

388 autoclave. The autoclave was sealed well and then placed in an oven. The
389 autoclave was heated up to 180℃ from room temperature with ramp rate of
390 3 ℃/min and then maintained at 180℃ for 4 hours. After, the autoclave was
391 removed from the oven and cooled to room temperature by running water
392 immediately. The resulting product was purified and washed with DI water
393 three times by centrifugation at 3000 r.p.m for 2 min. After washing and
394 purification, the final tellurium solution is a silver-gray color. Note that there
395 are always some Te nanowires coexisting along with Te nanoflakes and it is
396 challenging to fully separate the nanowires from the nanoflakes. The final
397 product was redispersed in pure ethanol before being transferred to the
398 target substrate for characterization and device fabrication by drop-casting.
399 Maintaining the autoclave in oven at 180℃ for 4h will produce the tellurium
400 nanoflakes with a typical thickness in the range of 10-30 nm, with typical
401 lateral dimensions of 10-50 μm. It is important to point out that the thickness
402 of tellurium nanoflakes can be roughly controlled by controlling the reaction
403 time (4-30 hours) at 180℃. The thickness of tellurium nanoflakes can be
404 increased by prolonging the reaction.

405 **Device Fabrication**

406 Te nanoflakes were transferred onto p^{++} Si/SiO_2 chips with a 50 nm oxide or
407 back reflector Al_2O_3/Au chips with varying thicknesses of Al_2O_3 by drop-
408 casting the tellurium ethanol solution. Back reflector substrates were
409 prepared by evaporating Ti/Au/Ti (10 nm/200 nm/1 nm) on Si substrates,
410 followed by atomic layer deposition of Al_2O_3 (Cambridge Nanotech). The final
411 Al_2O_3 thickness was determined by ellipsometry. Suitable Te nanoflakes were

412 then located on an optical microscope and devices were fabricated using
413 standard e-beam lithography techniques. After development, 40 nm thick Pd
414 was evaporated as electrode contacts *via* e-beam evaporation and lift-off
415 was performed using acetone.

416 **Material Characterization**

417 Transmission electron microscopy (TEM) images were performed at the
418 National Center for Electron Microscopy at Laurence Berkeley National
419 Laboratory using a FEI Titan 60–300 microscope operated at 200kV. Tapping
420 mode atomic force microscope (AFM) measurements were conducted on a
421 Dimension ICON AFM (Bruker, Germany) under ambient conditions. A AXS D8
422 Discover GADDS X-ray diffractometer (Bruker, Germany) equipped with a
423 Vantec-500 area detector and a Co Kα (λ=1.7903 Å) X-ray source was used
424 to measure the powder X-ray diffraction (XRD) pattern. The Raman spectrum
425 was measured on Horiba Jobin Yvon LabRAM ARAMIS automated scanning
426 confocal Raman microscope system with the excitation line of 532 nm
427 (Horiba, Ltd. Japan). The Raman band of a silicon wafer at 520 cm^{-1} was used
428 as the reference to calibrate the spectrometer.

429 **Optical/Electrical Characterization**

430 Samples for absorption/reflection measurements were transferred onto KBr
431 substrates using a previously established dry transfer technique and were
432 measured in an FTIR microscope (ThermoFisher).[35] Electrical measurements
433 were performed in a cryogenic protestation (LakeShore) with a B1500a
434 Semiconductor Parameter Analyzer (Agilent). Spectral photoresponse
435 measurements were performed in a FTIR spectrometer (ThermoFisher) with a

436 customized Janis cryostat equipped with a CaF_2 window. Devices were wire
437 bonded in a 24 pin chip carrier and evacuated to a base pressure of < 10^{-5}
438 Torr. The cryostat was then placed at the auxiliary exit port of the FTIR, and
439 the exciting illumination from the tungsten lamp source was focused on the
440 sample using either a CaF_2 lens or a 15× Schwarzschild objective. The optical
441 velocity of the FITR was set to either 0.1515 or 0.4747 cm s^{-1}; the resulting
442 modulation frequency range (7.5 kHz to 300 Hz) is within the operating
443 regime of the frequency response. The photocurrent from the Te devices was
444 then sent to a current amplifier (Stanford Research Systems), which also
445 provided the bias voltage. The resulting signal was subsequently returned to
446 the external detector interface of the FTIR. The relative intensity of the
447 illumination source was measured using the internal Deuterated Triglycine
448 Sulfate (DTGS) detector of the FTIR with identical measurement conditions.
449 The photoresponse was calibrated using a NIST traceable Ge photodiode
450 (ThorLabs) with a 100 µm aperture placed in the same position as the device
451 under measurement. The frequency response of the devices was measured
452 using a directly modulated 1550 nm laser diode. Further details and a
453 schematic of the measurement setup are provided in ref. 35.
454

455

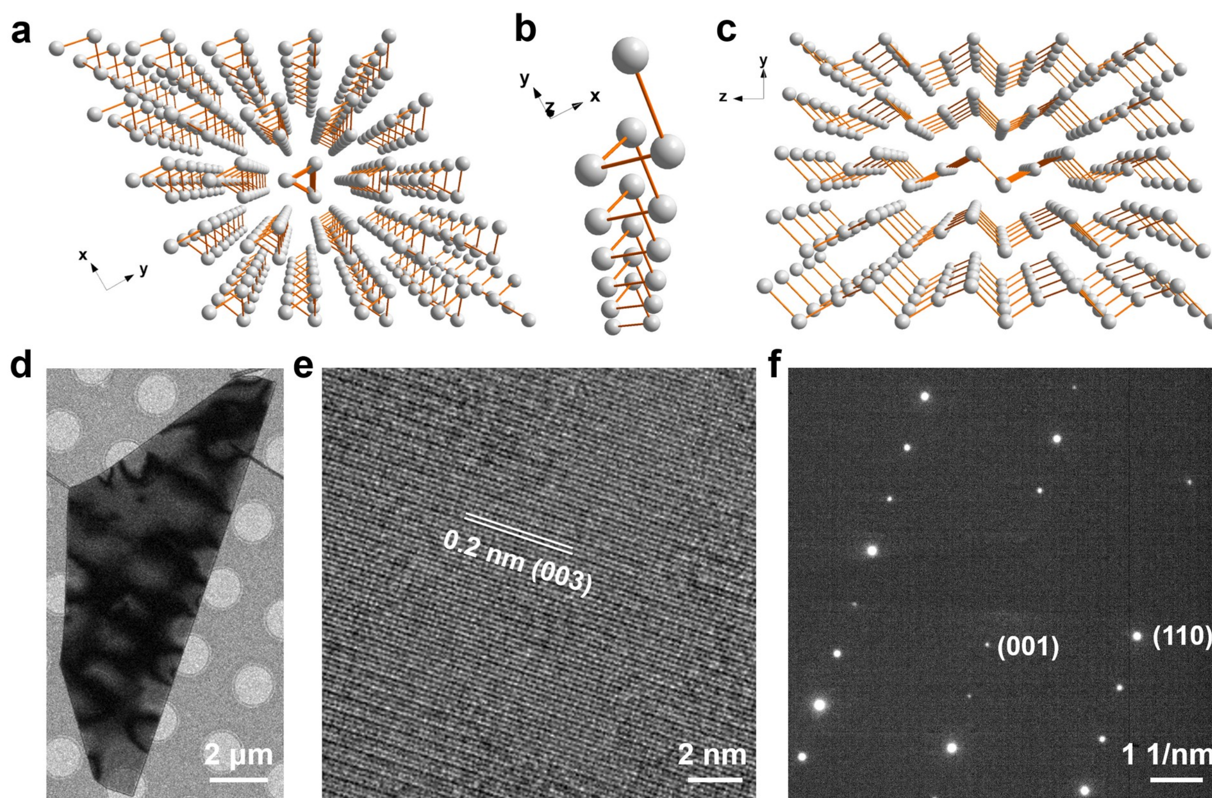

456 **Figure 1.** Crystal structure of tellurium: (a) viewed from x-axis, (b) single-
457 molecular chain and (c) viewed from z-axis. (d) TEM image, (e)
458 corresponding HR-TEM image and (f) SAED pattern of a typical tellurium
459 nanoflake.

460

461

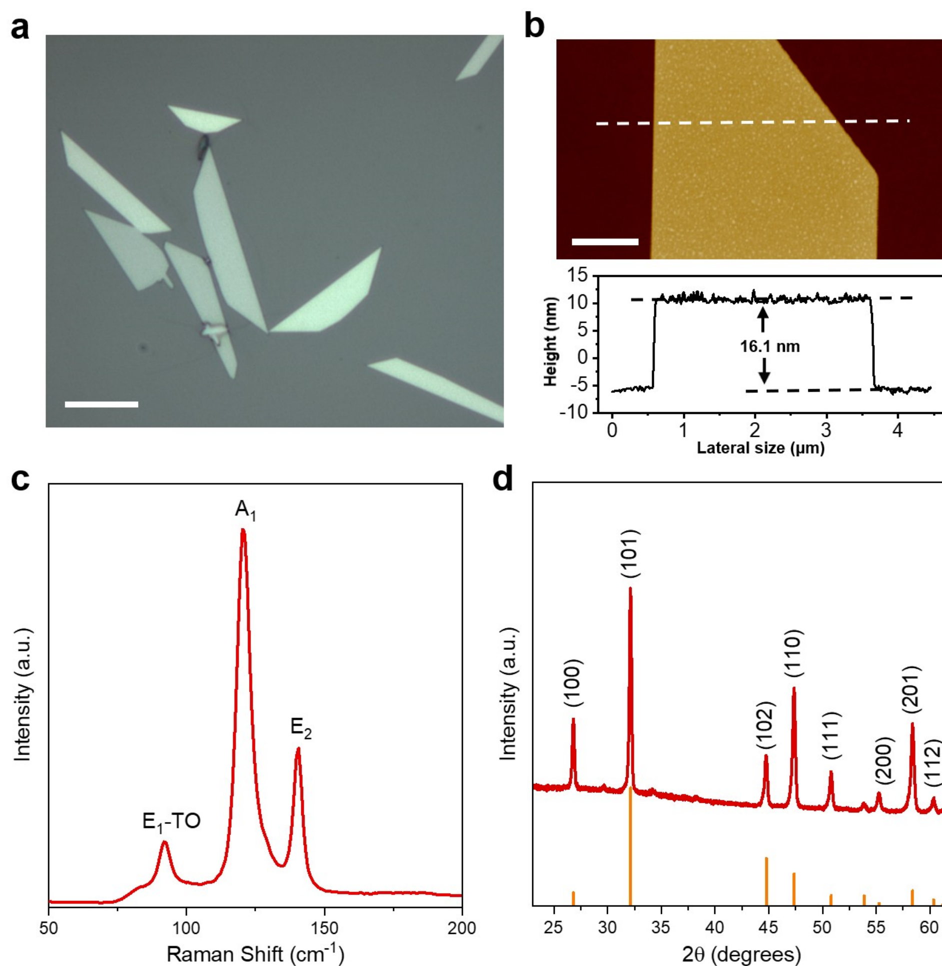

462 **Figure 2.** (a) Optical microscope image of tellurium nanoflakes deposited on
463 a SiO_2/Si substrate, scale bar is 10 μm. (b) AFM image of typical tellurium
464 nanoflake (top) and the corresponding height profile (bottom), scale bar is 1
465 μm. (c) Raman spectrum of tellurium nanoflakes. (d) XRD pattern of dried
466 tellurium nanoflake powder.

467

468

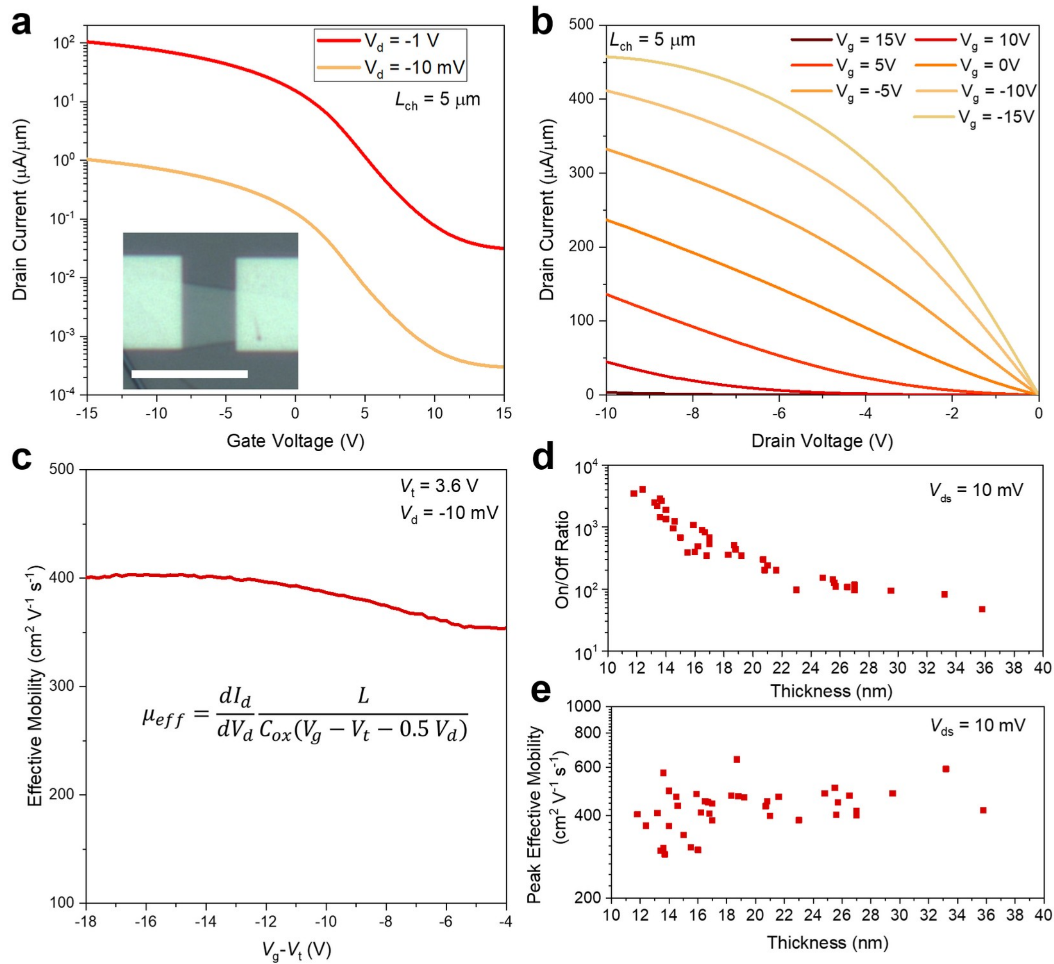

469 **Figure 3.** (a) Back-gated I_d-V_g characteristics of a 12.3 nm thick Te
470 nanoflake with Pd contacts on 50 nm SiO_2 measured at room temperature;
471 inset shows optical image of the device, scale bar is 10 μm. (b) I_d-V_d
472 measured for the same device as shown in panel (a). (c) Effective mobility as
473 a function of gate overdrive voltage for the device shown in panel (a) under
474 a V_d of -10 mV, giving a peak mobility value of 619 cm^{-2} V^{-1} s^{-1}. (d) Thickness
475 dependence of the on/off ratio measured for Te nanoflakes of varying
476 thickness in the range of 12-36 nm. (e) Thickness dependence of the peak
477 effective mobility measured for Te nanoflakes of varying thickness in the
478 range of 12-36 nm.

479

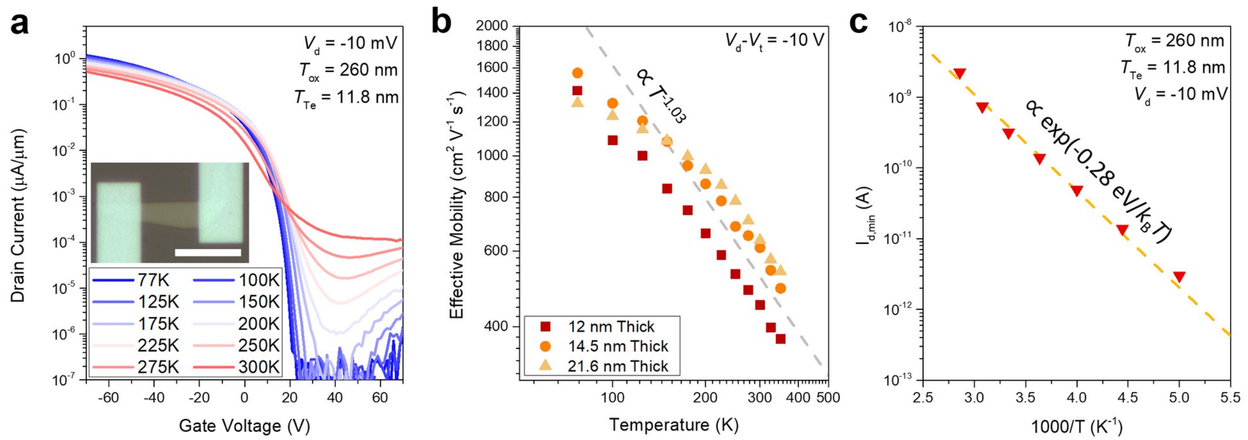

480

481 **Figure 4.** (a) Temperature dependent I_d-V_g characteristics of a 12 nm thick
482 Te nanoflake, measured at a low V_d of -10 mV. Scale bar is 5 μm. (b)
483 Effective mobility for quasi-2D Te nanoflakes with varying thickness as a
484 function of temperature extracted from panel (a) and Figure S1 at a constant
485 gate overdrive voltage of -10 V, dashed line shows a power law fit. (c)
486 Arrhenius plot showing the minimum drain source current ($I_{d,min}$) as a function
487 of temperature extracted from the data shown in panel (a).

488

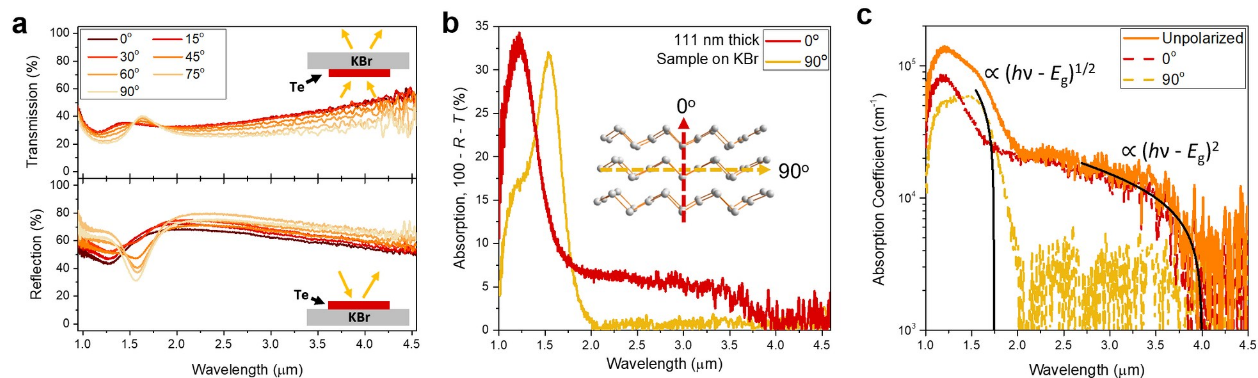

Figure 5. (a) Polarization resolved transmission and reflection spectra measured for a 111 nm thick Te nanoflake transferred on a KBr substrate, insets show the optical configuration used during measurements. (b) Absorption spectra for the nanoflake measured in panel (a), calculated from 100%-*T*-*R*. Inset shows the Te crystal directions of 0° and 90°. (c) Absorption coefficient of tellurium for unpolarized light, as well as light aligned parallel to z-axis (0°) and y-axis (90°) of Te crystal; Tauc plots and optical bandgap extraction for light polarized perpendicular and parallel to the wire axis are shown in Figure S2.

499

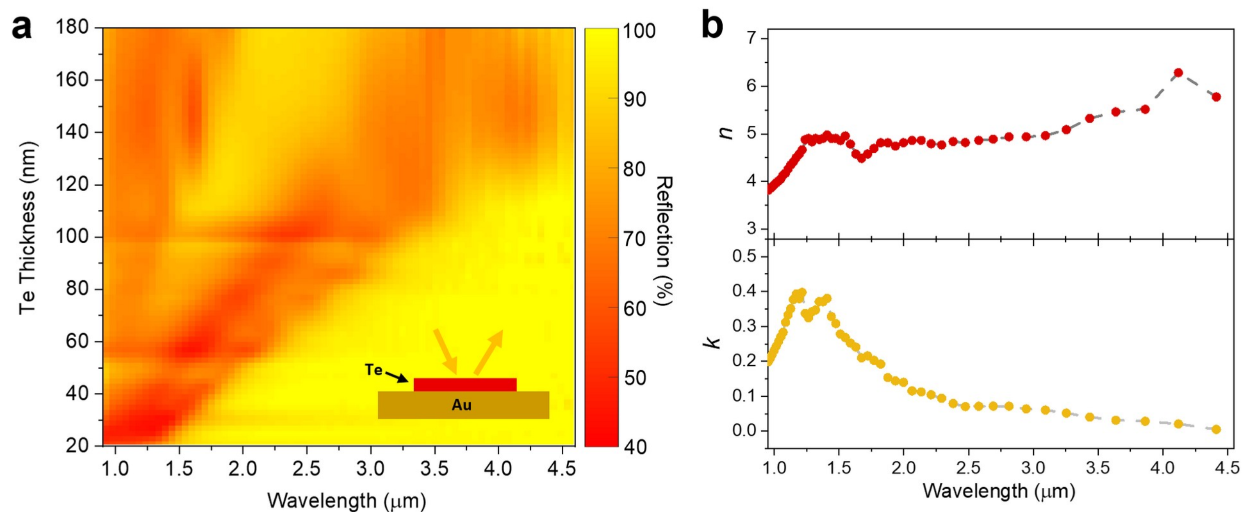

500 **Figure 6.** (a) Reflection of quasi-2D Te nanoflakes on Au substrates, with Te
501 thickness ranging from 20 nm to 180 nm. Plot is obtained from interpolation
502 of spectra taken on 18 Te crystal nanoflakes of varying thicknesses, shown in
503 Figure S3. (b) Complex refractive index of quasi-2D Te nanoflakes calculated
504 by fitting measured reflection data as a function of thickness.

505

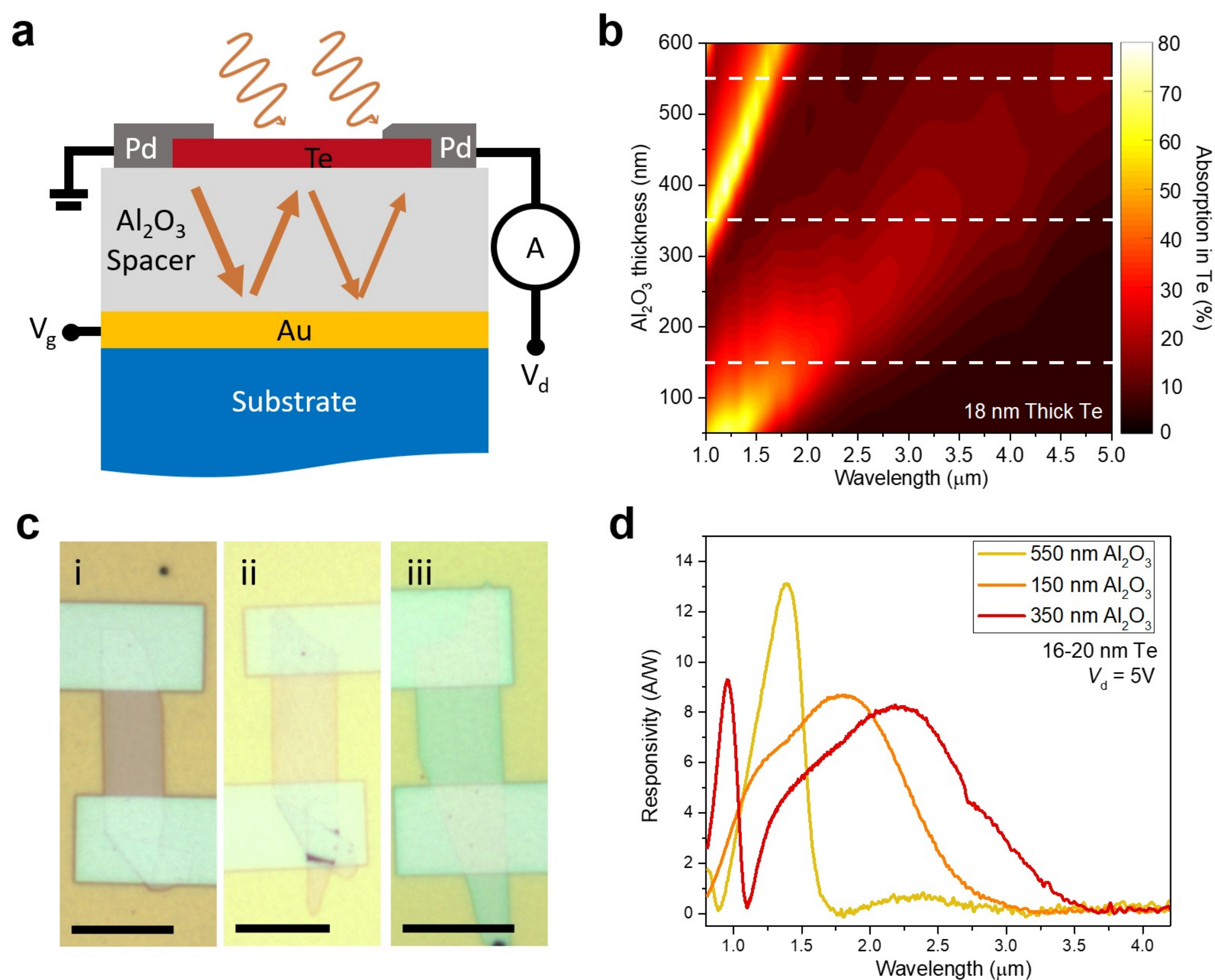

506

507 **Figure 7.** (a) Schematic showing the optical cavity structure used to
508 fabricate SWIR photoconductors from quasi-2D Te nanoflakes in this study.
509 An evaporated Au film acts as the gate electrode and back-reflector, while a
510 Al_2O_3 dielectric layer acts as a ~λ/4 spacer as well as the gate oxide. (b)
511 Calculated absorption in the Te layer, as a function of wavelength and Al_2O_3
512 thickness for a fixed semiconductor thickness of 18 nm. (c) Optical images of
513 SWIR photoconductors fabricated on optical cavities with Al_2O_3 thickness of
514 550 nm (i), 150 nm (ii), and 350 nm (iii); scale bar is 10 μm. (d) Measured

515 responsivities of quasi-2D Te nanoflakes fabricated on optical cavities with

516 different Al_2O_3 thicknesses.

517

518

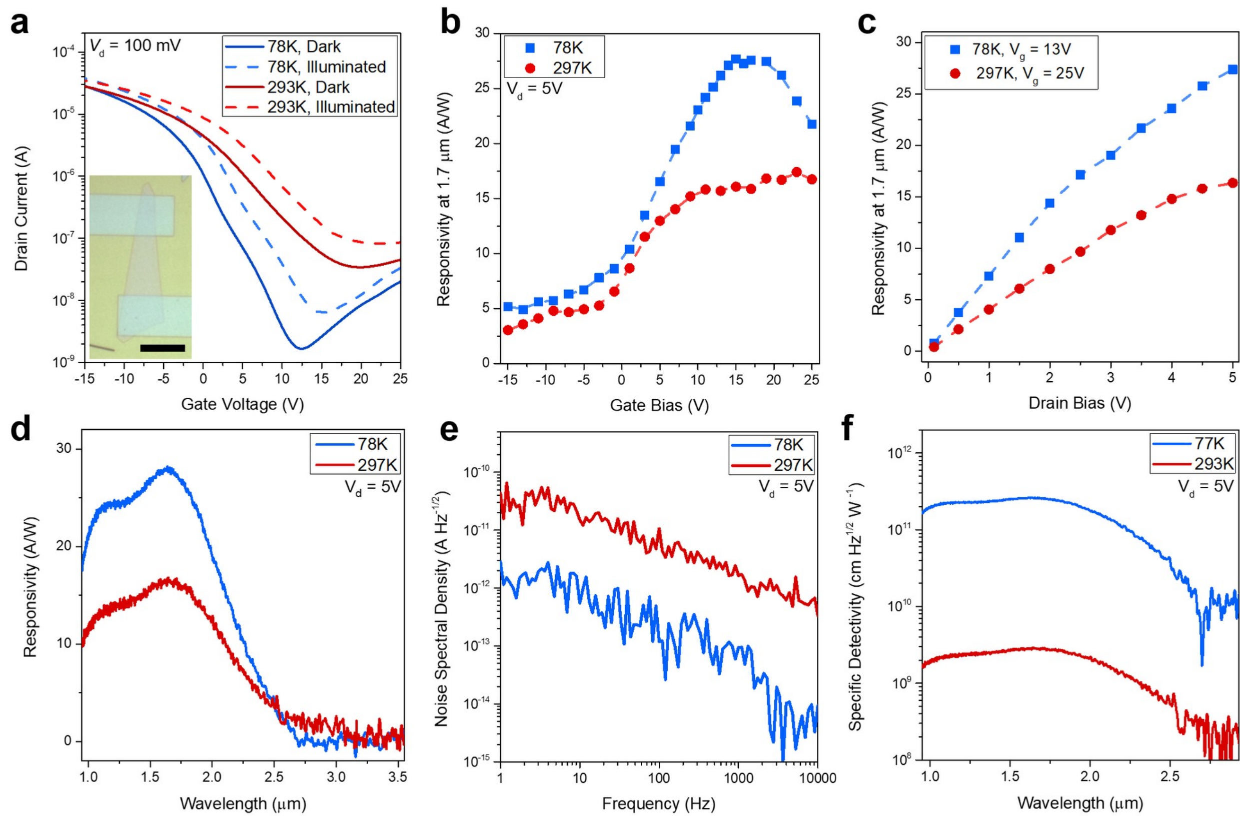

519 **Figure 8.** (a) I_d-V_g characteristics of an 18.8 nm Te photoconductor
520 measured at 297K and 78K under illumination and in the dark. Inset shows
521 optical image of the measured device; scale bar is 10 μm. (b) Responsivity at
522 1.7 μm measured at 297K and 78K as a function of gate bias, at a constant
523 drain bias of V_d = 5 V. (c) Responsivity at 1.7 μm measured at 297K and 78K
524 as a function of drain bias at an optimized gate bias (V_g = 13 V at 78K and V_g
525 = 25 V at 297K). (d) Spectral responsivity per watt of a Te photoconductor
526 measured at 78K and 297K under optimized gate bias and V_d = 5 V. (e) Noise
527 spectrum measured at room temperature for a Te photoconductor operated
528 with optimized gate bias and a V_d = 5 V and optimized gate bias. (f) Specific
529 detectivity of Te photoconductors with optimized thickness; measurements
530 were performed under gating conditions which maximized detectivity for the

531 specific device at room temperature. Note that an Au/Al_2O_3 substrate with an

532 Al_2O_3 thickness of 150 nm was used for the measurements.

533

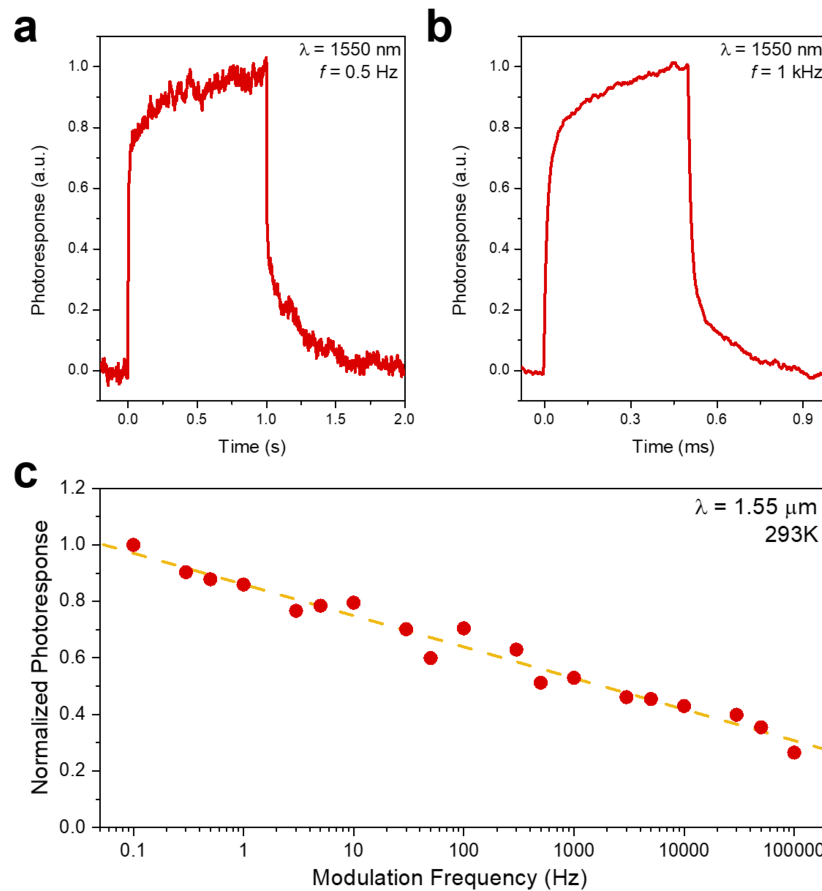

534

535 **Figure 9.** (a) Room-temperature step response of an 18.8nm thick Te

536 photoconductor, excited by a 1550-nm laser modulated by a 0.5 Hz square

537 wave. (b) Room-temperature step response of a Te photoconductor, excited

538 by a 1550 nm laser modulated by a 1 kHz square wave. (c) Normalized

539 photoresponse of a Te photoconductor *versus* modulation frequency; the

540 device is excited using a sinusoidally modulated 1550 nm laser. Note that an

541 Au/Al_2O_3 substrate with an Al_2O_3 thickness of 150 nm was used for the

542 measurements.

543

544

545

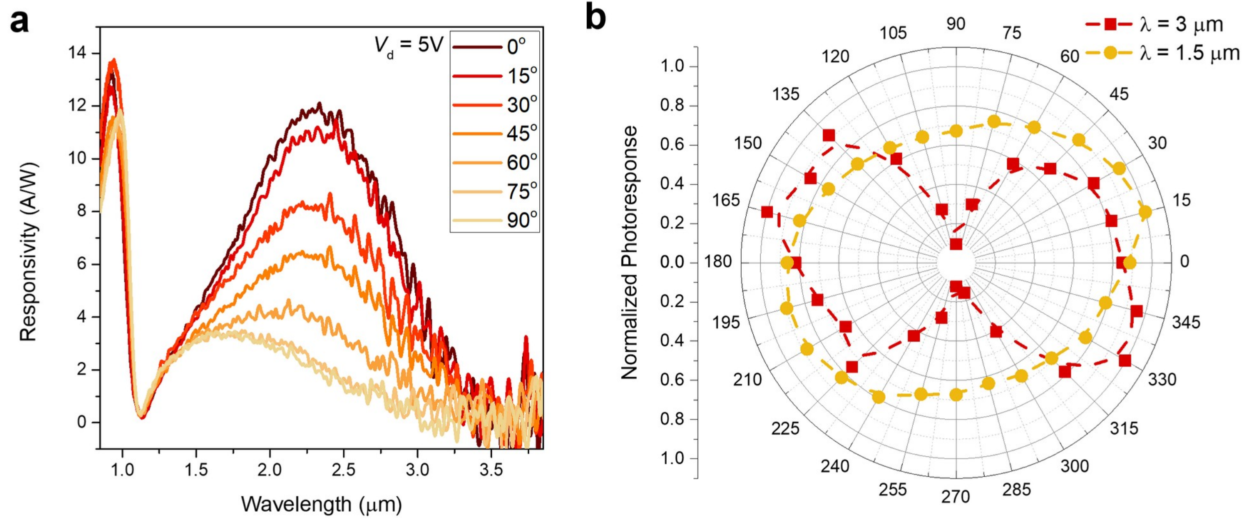

546 **Figure 10.** (a) Polarization resolved photoresponse of an 18.8 nm thick
547 quasi-2D Te nanoflake fabricated on an optical cavity with a 350 nm thick
548 Al_2O_3. (b) Polar plot showing the relative response of the device shown in
549 panel (a) at wavelengths of 3 μm and 1.5 μm as a function of polarization.

550

551

TOC Graphic

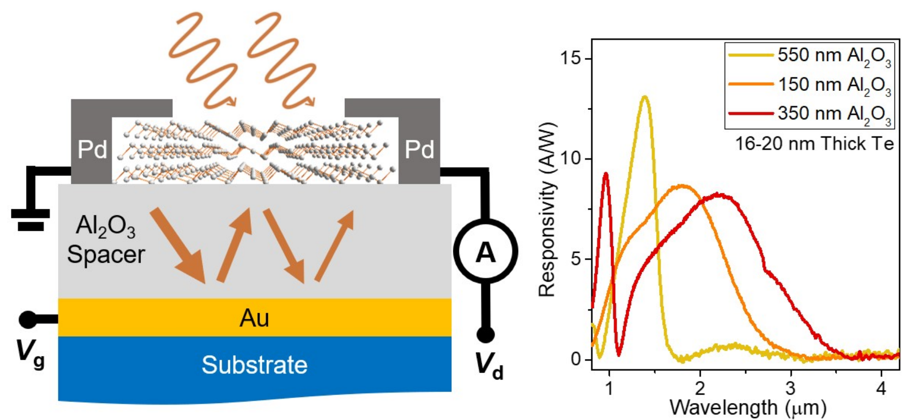

552

553

554 ASSOCIATED CONTENT

555 **Supporting Information**

556 The Supporting Information is available free of charge on the ACS
557 Publications website.

558 Temperature dependent electrical characterization of additional
559 devices. Tauc plot used to extract direct and indirect bandgap of Te.
560 Reflection spectra used to create plot in Fig. 6a. Photoresponse
561 measurements for devices prepared on Si/SiO_2 substrates. Reflection
562 spectra taken on Te photoconductors.

563 AUTHOR INFORMATION

564 **Corresponding Author**

565 *E-mail: ajavey@berkeley.edu
566

567 **ORCID**

568 Matin Amani: 0000-0002-7912-6559

569 Chaoliang Tan: 0000-0003-1695-5285

570 George Zhang: 0000-0002-1741-5267

571 James Bullock: 0000-0001-7903-9642

572 Xiaohui Song: 0000-0001-7713-1373

573 Vivek Raj Shrestha: 0000-0002-7731-7677

574 Yang Gao: 0000-0002-9004-8483

575 Kenneth Crozier: 0000-0003-0947-001X

576 Mary Scott: 0000-0002-9543-6725

577 Ali Javey: 0000-0001-7214-7931

578

579 **ACKNOWLEDGEMENT**

580 Device fabrication and measurements were supported by the Defense
581 Advanced Research Projects Agency under contract no. HR0011-16-1-0004.
582 Synthesis work was supported by the U.S. Department of Energy, Office of
583 Science, Office of Basic Energy Sciences, Materials Sciences and Engineering
584 Division under contract no. DE-AC02-05CH11231 within the Electronic
585 Materials Program (KC1201). Work at the Molecular Foundry was supported

586 by the Office of Science, Office of Basic Energy Sciences, of the U.S.
587 Department of Energy under Contract No. DE-AC02-05CH11231.
588

589 **References**

590 1. Alamo, J. A. Nanometre-Scale Electronics with III-V Compound
591 Semiconductors. *Nature* **2011**, 479, 317-323.
592 2. Chuang, S.; Gao, Q.; Kapadia, R.; Ford, A. C.; Guo, J.; Javey, A. Ballistic InAs
593 Nanowire Transistors. *Nano Lett.* **2012**, 13, 555-558.
594 3. Barve, A. V.; Lee, S. J.; Noh, S. K.; Krishna, S. Review of Current Progress in
595 Quantum Dot Infrared Photodetectors. *Laser Photon. Rev.* **2009**, 4, 738-
596 750.
597 4. Hoang, A. M.; Dehzangi, A.; Adhikary, S.; Razeghi, M. High Performance
598 Bias-Selectable Three-Color Short-Wave/Mid-Wave/Long-Wave in Infrared
599 Photodetecotrs based on Type-II InAs/GaSb/AlSb Superlattices. *Sci. Rep.*
600 **2016**, 6, 24144.
601 5. Martyniuk, P.; Antoszewski, J.; Martyniuk, M.; Faraone, L.; Rogalski, A. New
602 Concepts in Infrared Photodetector Designs. *Appl. Phys. Rev.* **2014**, 1,
603 041102.
604 6. Martinelli, R. U.; Zamerowski, T. J.; Longeway, P. A. 2.6 μm InGaAs
605 Photodiodes. *Appl. Phys. Lett.* **1988**, 53, 989-991.
606 7. Nishida, K.; Taguchi, K.; Matsumoto, Y. InGaAsP Heterostructure Avalanche
607 Photodiodes With High Avalanche Gain. *Appl. Phys. Lett.* **1979**, 35, 251-
608 253.
609 8. Chen, K.; Kapadia, R.; Harker, A.; Desai, S.; Kang, J. S.; Chuang, S.; Tosun,
610 M.; Sutter-Fella, C. M.; Tsang, M.; Zeng, Y.; Kiriya, D.; Hazra, J.;
611 Madhvapathy, S. R.; Hettick, M.; Chen, Y.-Z.; Mastandrea, J.; Amani, M.;
612 Cabrini, S.; Chueh, Y.-L.; Ager, J. W.; Chrzan, D. C.; Javey, A. Direct Growth

613 of Single Crystalline III-V Semiconductors on Amorphous Substrates. *Nat.*
614 *Comm.* **2016**, 7, 10502.
615 9. Ko, H.; Takei, K.; Kapadia, R.; Chuang, S.; Fang, H.; Leu, P. W.; Ganapathi,
616 K.; Plis, E.; Chen, S.-Y.; Madsen, M.; Ford, A. C.; Chueh, Y.-L.; Krishna, S.;
617 Salahuddin, S.; Javey, A. Ultrathin Compound Semiconductor on Insulator
618 Layers for High-Performance Nanoscale Transistors. *Nature* **2010**, 468,
619 286-289.
620 10. Fitzgerald, E. A.; Xie, Y.-H.; Monroe, D.; Silverman, P. J.; Kuo, J. M.;
621 Kortan, A. R.; Thiel, F. A.; Weir, B. E. Relaxed Ge_xSi_{1-x} Structures for III-V
622 Integration with Si and High Mobility Two-Dimensional Electron Gasses in
623 Si. *J. Vac. Sci. Technol. B* **1992**, 10, 1807-1819.
624 11. Kim, Y.; Cruz, S. S.; Lee, K.; Alawode, B. O.; Choi, C.; Song, Y.; Johnson, J.
625 M.; Heidelberger, C.; Kong, W.; Choi, S.; Qiao, K.; Almansouri, I.; Fitzgerald,
626 E. A.; Kong, J.; Kolpak, A. M.; Hwang, J.; Kim, J. Remote Epitaxy Through
627 Graphene Enables Two-Dimensional Material-Based Layer Transfer. *Nature*
628 **2017**, 554, 340-343.
629 12. Li, T.; Cheng, J.-F.; Shao, X.-M.; Deng, H.-H.; Chen, Y.; Tang, H.-J.; Li, X.;
630 Gong, H.-M. Performance of Low Dark Current InGaAs Shortwave Infrared
631 Detector. *Proc. SPIE.* **2012**, 8419.
632 13. Tan, C.; Cao, X.; Wu, X.-J.; He, Q.; Yang, J.; Zhang, X.; Chen, J.; Zhao, W.;
633 Han, S.; Nam, G.-H.; Sindoro, M.; Zhang, H. Recent Advances in Ultrathin
634 Two-Dimensional Materials. *Chem. Rev.* **2017**, 117, 6225-6331.
635 14. Lin, Z.; McCreary, A.; Briggs, N.; Subramanian, S.; Zhang, K.; Sun, Y.; Li,
636 X.; Borys, N. J.; Yuan, H.; Fullerton-Shirey, S. K.; Chernikov, A.; Zhao, H.;

637 McDonnell, S.; Lindenberg, A. M.; Xiao, K.; LeRoy, B. J.; Drndić, M.; Hwang, J. C.M.; Park, J.; Chhowalla, M.; *et al*. 2D Materials Advances: From Large Scale Synthesis and Controlled Heterostructures to Improved Characterization Techniques, Defects and Applications. *2D Mater*. **2016**, 3, 042001.

15. Amani, M.; Lien, D.-H.; Kiriya, D.; Xiao, J.; Azcatl, A.; Noh, J.; Madhvapathy, S. R.; Addou, R.; Kc, S.; Dubey, M.; Cho, K.; Wallace, R. M.; Lee, S.-C.; He, J.-H.; Ager, J. W.; Zhang, X.; Yablonovitch, E.; Javey, A. Near-Unity Photoluminescence Quantum Yield in MoS_2. *Science* **2015**, 350, 1065-1068.

16. Amani, M.; Taheri, P.; Addou, R.; Ahn, G. H.; Kiriya, D.; Lien, D.-H.; Ager, J. W.; Wallace, R. M.; Javey, A. Recombination Kinetics and Effects of Superacid Treatment in Sulfur- and Selenium Based Transition Metal Dichalcogenides. *Nano Lett.* **2016**, 16, 2786-2791.

17. Desai, S. B.; Madhvapathy, S. R.; Sachid, A. B.; Llinas, J. P.; Wang, Q.; Ahn, G. H.; Pitner, G.; Kim, M. J.; Bokor, J.; Hu, C.; Wong, H.-S. P.; Javey, A. MoS_2 Transistors with 1-Nanometer Gate Lengths. *Science* **2016**, 354, 99-102.

18. Lien, D.-H.; Amani, M.; Desai, S. B.; Ahn, G. H.; Han, K.; He, J.-H.; Ager, J. W.; Wu, M. C.; Javey, A. Large-Area and Bright Pulsed Electroluminescence in Monolayer Semiconductors. *Nat. Comm.* **2018**, 9, 1299.

19. Zhang, Y. J.; Oka, T.; Suzuki, R.; Ye, J. T.; Iwasa, Y. Electrically Switchable Chiral Light-Emitting Transistor. *Science* **2014**, 344, 725-728.

661 20. Zhao, P.; Amani, M.; Lien, D.-H.; Ahn, G. H.; Kiriya, D.; Mastandrea, J. P.;
662 Ager, J. W.; Yablonovitch, E.; Chrzan, D. C.; Javey, A. Measuring the Edge
663 Recombination Velocity of Monolayer Semiconductors. *Nano Lett.* **2017**,
664 17, 5356-5360.
665 21. Wang, Y.; Qiu, G.; Wang, R.; Huang, S.; Wang, Q.; Liu, Y.; Du, Y.;
666 Goddard, W. A.; Kim, M. J.; Xu, X.; Ye, P. D.; Wu, W. Field-Effect Transistors
667 made from Solution-Grown Two-Dimensional Tellurene. *Nat. Electron.*
668 **2018**, 1, 228-236.
669 22. von Hippel, A. Structure and Conductivity in the VIb Group of the
670 Periodic System. *J. Chem. Phys.* **1948**, 16, 372-380.
671 23. Yi, S.; Zhu, Z.; Cai, X.; Jia, Y.; Cho, J.-H. The Nature of Bonding in Bulk
672 Tellurium Composed of One-Dimensional Helical Chains. *Inorg. Chem.*
673 **2018**, DOI: 10.1021/acs.inorgchem.7b03244.
674 24. Wu, B.; Liu, X.; Yin, J.; Lee, H. Bulk β-Te to Few Layered β-Tellurenes:
675 Indirect to Direct Band-Gap Transitions Showing Semiconductor Property.
676 *Mater. Res. Express* **2017**, 4,095902.
677 25. Qian, H.; Yu, S.; Gong, J.; Luo, L.; Fei, L. High-Quality Luminescent
678 Tellurium Nanowires of Several Nanometers in Diameter and High Aspect
679 Ratio Synthesized by a Poly(Vinyl Pyrrolidone)-Assisted Hydrothermal
680 Process. *Langmuir* **2006**, 22, 3830-3835
681 26. Du, Y.; Qiu, G.; Wang, Y.; Si, M.; Xu, X.; Wu, W.; Ye, P. D. 1D van der
682 Waals Material Tellurium: Raman Spectroscopy under Strain and Magneto-
683 transport
684 Source. *Nano Lett.* **2017**, 17, 3965-3973.

685 27. Liu, H.; Neal, A. T.; Zhu, Z.; Luo, Z.; Xu, X.; Tomanek, D.; Ye, P. D.
686 Phosphorene: An Unexplored 2D Semiconductor with a High Hole Mobility.
687 *ACS Nano* **2014**, 8, 4033-4041.
688 28. Li, L.; Yu, Y.; Ye, G. J.; Ge, Q.; Ou, X.; Wu, H.; Feng, D.; Chen, X. H.;
689 Zhang, Y. Black Phosphorus Field-Effect Transistors. *Nat. Nano.* **2014**, 9,
690 372-377.
691 29. Takei, K.; Madsen, M.; Fang, H.; Kapadia, R.; Chuang, S.; Kim, H. S.; Liu,
692 C.-H.; Plis, E.; Nah, J.; Krishna, S.; Chueh, Y.-L. Guo, J.; Javey, A. Nanoscale
693 InGaSb Heterostructure Membranes on Si Substrates for High Hole
694 Mobility Transistors. *Nano Lett.* **2012**¸12, 2060-2066.
695 30. Radisavljevic, B.; Kis A. Mobility Engineering and a Metal-Insulator
696 Transition in Monolayer MoS_2. *Nat. Matter.* **2013**, 12, 815-820.
697 31. Javey, A.; Guo, J.; Farmer, D. B.; Wang, Q.; Wang, D.; Gordon, R. C.;
698 Lundstrom, M.; Dai, H. Carbon Nanotube Field-Effect Transistors with
699 Integrated Ohmic Contacts and High-κ Gate Dielectrics. *Nano Lett.* **2004**,
700 4, 447-450.
701 32. Lien, D.-H.; Kang, J. S.; Amani, M.; Chen, K.; Tosun, M.; Wang, H.-P.; Roy,
702 T.; Eggleston, M. S.; Wu, M. C.; Dubey, M.; Lee, S.-C.; He, J.-H.; Javey, A.
703 Engineering Light Outcoupling in 2D Materials. *Nano Lett.* **2015**, 15, 1356-
704 1361.
705 33. Zhang, H.; Ma, Y.; Wan, Y.; Rong, X.; Xie, Z.; Wang, W.; Dai, L. Measuring
706 the Refractive Index of Highly Crystalline, Monolayer MoS_2 with High
707 Confidence. *Sci. Rep.* **2015**, 5, 8440.
708 34. Born, M.; Wolf. E. Principles of optics: Electromagnetic Theory of

Propagation, Interference and Diffraction Light. Cambridge University Press, Cambridge (2002).

35. Amani, M.; Regan, E.; Bullock, J.; Ahn, G. H.; Javey, A. Mid-Wave Infrared Photoconductors based on Black Phosphorous-Arsenic Alloys. *ACS Nano* **2017**, 11, 11724-11731.

36. Guo, Q.; Pospischil, A.; Bhuiyan, M. Jiang, H.; Tian, H.; Farmer, D.; Deng, B.; Li, C.; Han, S.-J.; Wang, H.; Xia, Q.; Ma, T.-P. Mueller, T.; Xia, F. Black Phosphorus Mid-Infrared Photodetectors with High Gain. *Nano Lett.* **2016**, 16, 4648-4655.

37. Piotrowski, J.; Gawron, W. Ultimate Performance of Infrared Photodetectors and Figure of Merit of Detector Material. *Infar. Phys. Technol.* **1997**, 38, 63-68.

38. Vincent, J. D. Fundamentals of Infrared Detector Operation and Testing. Wiley, New York (1990).

39. Petritz, R. L. Theory of Photoconductivity in Semiconductor Film. *Phys. Rev.* **1956**, 104, 1508-1516.

40. Beck, W. A. Photoconductive Gain and Generation-Recombination Noise in Multiple-Quantum-Well Infrared Detectors. *Appl. Phys. Lett.* **1993**, 63, 3589-3591.

41. Ye, Z.; Campbell, J. C.; Chen, Z.; Kim, E.-T., Madhukar, A. Noise and Photoconductive Gain in InAs Quantum-Dot Infrared Photodetectors. *Appl. Phys. Lett.* **2003**, 83, 1234-1236.